Journal of
Materials Chemistry A

Materials for energy and sustainability

Accepted Manuscript

This article can be cited before page numbers have been issued, to do this please use: M. Nasir Hussain, N. Buday, S. G. Hickey, U. Shamraiz, C. A. Howard, X. Ji and S. Yasar, *J. Mater. Chem. A*, 2026, DOI: 10.1039/D6TA01424K.

ROYAL SOCIETY OF CHEMISTRY

rsc.li/materials-a

View Article Online
DOI: 10.1039/D6TA01424K

MOF-Derived Chalcogenides Multifunctional Heterostructure Materials for High-Performance Supercapacitor and Oxygen Evolution Reaction Catalytic Activity

Muhammad Nasir Hussain[a]*, Nesrin Bugday[a], Stephen G. Hickey[b], Umair Shamraiz[c], Christopher A. Howard[d], Xiaobo Ji[e] and Sedat Yaşar[a]*

[a] İnönü University, Faculty of Science and Art, Department of Chemistry, 44280, Malatya, Türkiye.

[b]School of Chemistry and Biosciences, University of Bradford, BD7 1DP, United Kingdom.

[c]Department of Chemistry, Quaid-i-Azam University, Islamabad, 45320, Pakistan.

[d]Department of Physics & Astronomy, University College London, London WC1E 6BT, U.K.

[e]Deanship of Scientific Research, Imam Mohammad Ibn Saud Islamic University (IMSIU), Riyadh, Saudi Arabia.

[f]Central South University, College of Chemistry and Chemical Engineering, 410083, Changsha, China.

*Corresponding author, Muhammad Nasir Hussain, e-mail: nasir.hussain@inonu.edu.tr;
Sedat Yaşar, e-mail: sedat.yasar@inonu.edu.tr

Abstract

Conventional electrode materials are generally optimized for a specific function, and therefore often possess one or more of the following: low electrical conductivity, less active site utilization, sluggish ion-electron kinetics, and poor structural stability, thus limiting their multifunctional viability. Therefore, we report the synthesis of a series of ZIF-12-derived, post-synthesis metal-modified composite heterostructures: Cu/Zn/Co@NPC, Cu_2Se/ZnSe/$CoSe_2$@NPC, and Cu_2S/ZnS/CoS_2@NPC achieved through direct thermal treatment of the MOF under an inert atmosphere. The synthesized composites are comprehensively investigated for supercapacitor and oxygen evolution reaction applications. Among all the fabricated composites, Cu_2S/ZnS/CoS_2@NPC demonstrates the highest specific capacitance of 1206 F g^{-1} at 1 A g^{-1}, outperforming both the Cu/Zn/Co@NPC (620 F g^{-1}) and Cu_2Se/ZnSe/$CoSe_2$@NPC (894 F g^{-1}). The low charge transfer resistance of 0.175 Ω for Cu_2S/ZnS/CoS_2@NPC is indicative of enhanced electrical conductivity and facile charge transport. An asymmetric supercapacitor device

View Article Online
DOI: 10.1039/D6TA01424K

assembled using $Cu_2S/ZnS/CoS_2$@NPC achieves a specific capacitance of 114 F g^{-1} at 3 A g^{-1} and delivered an energy density of 15.83 Wh kg^{-1} at a power density of 1.5 kW kg^{-1} with capacity retention of 92.1% over 6000 cycles. Additionally, Cu/Zn/Co@NPC, $Cu_2Se/ZnSe/CoSe_2$@NPC, and $Cu_2S/ZnS/CoS_2$@NPC exhibit overpotentials of 150, 140, and 120 mV at 10 mA cm^{-2} whose Tafel slopes are 180, 103, and 92 mV dec^{-1}, respectively. The bifunctional $Cu_2S/ZnS/CoS_2$@NPC composite demonstrates superior performance which can be assigned to its enhanced electrical conductivity, abundant redox active sites, superior heterointerfaces, and robust architecture all of which facilitate rapid charge transfer. This work demonstrates the potential of MOF-derived multimetal chalcogenide heterostructures embedded in nitrogen doped porous carbon to act as efficient and multifunctional electrode materials for energy storage and conversion technologies.
Keywords: MOF, Supercapacitor, OER, Energy storage, Multimetal chalcogenides.

Introduction

Electrochemical energy storage and conversion (EESC) technologies are considered as essential components to overcome the growing global energy crisis and associated environmental issues due to their favorable energy efficiency and low ecological impact. Recently, EESC systems such as supercapacitors (SCs), batteries, fuel cells, water electrolysis, and carbon dioxide reduction reactions (CO_2RR) have all been extensively investigated.[1, 2] Among these technologies, supercapacitors (SCs) have been demonstrated to fill the gap between conventional capacitors and batteries by offering significantly higher power densities and longer cycle lives than batteries even if at lower energy density.[3] The storage behavior in SCs is primarily based on two mechanisms, the electrochemical double layer (EDLC) and pseudocapacitance. In EDLC, charge is stored electrostatically due to the adsorption of ions at the electrode-electrolyte interface with enhanced stability and fast ion kinetics. On the other hand, pseudocapacitors store charges via fast and reversible Faradaic reactions which occur at or near surfaces, resulting in a high energy density.[4] Additionally, various materials demonstrate an intercalation-type, pseudocapacitive phenomenon in which ions are inserted into the inner structure of the electrode without phase changes, and show a battery-type energy density with capacitor like rate capability.[5] Despite having many advantages, SCs still face inherent limitations which prevent their widespread adoption. The low energy density of 5-20 Wh kg^{-1} compared to that of lithium-ion batteries (100–265 W h kg^{-1}) results in a bulkier device configuration upon scale-up.[6] Their low operating voltage, especially in aqueous

View Article Online
DOI: 10.1039/D6TA01424K

electrolytes, often requires multiple cells to be connected in series to achieve practical working voltages which increases the cost and complexity of the system. Electrolyte instability at high voltages and the cost of electrode materials further limits commercial viability.[7] These challenges therefore underscore the need for innovation in materials development and device modification to elevate the practical performance of SCs. The key to achieving greater electrochemical performance in SCs lies in electrode materials that support fast ion and electron transport, provide abundant redox-active sites, and maintain structural stability during charge-discharge cycles.[8]

This is also true of electrocatalytic processes such as the oxygen evolution reaction (OER) which plays a key role in water splitting, rechargeable metal-air batteries, fuel cells, and CO_2RR devices.[9-11] The OER is a very sluggish multielectron transfer process which is accompanied by the complex formation of intermediates that frequently influences the overall energy efficiency of the device. A main advantage of OER systems is that they result in the production of green hydrogen when combined with the hydrogen evolution reaction (HER). This strategy supports carbon-free energy conversion while playing an important role in regenerative fuel cells and energy storage.[12] Recently, efforts have been devoted toward noble-metal free catalysts which can reduce cost and enable scalability.[13] The major challenges facing the OER are that of energy loss due to high over potential,[14] catalyst instability in acidic media, gas crossover, and production of reactive oxygen species which also raises safety concerns.[15, 16] Therefore, the design of bifunctional or multifunctional electrode materials with the capability of performing both energy storage and conversion activities is highly desirable. These multifunctional materials can offer fast and reversible charge storage, effective ion-electron transportation, and more active sites in a single architecture. This integrated functionality can not only minimize the redundancy and device complexity but also enable the fabrication of compact and hybrid energy systems including metal-air batteries, SC-electrolyzers, and renewable energy units, where energy storage and conversion processes function synergistically.

It is nontrivial to achieve both high capacitance and OER activity because SCs require a large surface area, porous structure, and smooth diffusion of ions while OER catalysts require stable active sites, fast electron transfer kinetics, and strong catalytic centers. To reconcile these demands the most promising approach is to develop heterostructures, such as multimetal chalcogenides/carbon composites derived from metal-organic frameworks (MOFs) precursors.[17-19] MOFs are a unique class of porous materials with high crystallinity and long-range structural

View Article Online
DOI: 10.1039/D6TA01424K

order which are interconnected through coordination bonds of metal ions/clusters and organic ligands.[20] Unlike pristine MOFs, MOF-derived materials have drawn significant interest in different EESC devices due to their excellent stability, high electronic conductivity, and elevated electrochemical performance.[11] For instance, MOF-derived metal chalcogenides (selenides and sulfides) integrated with heteroatom-doped carbon matrices have gained widespread attention as they fulfill the requirements of transition metal redox chemistry and conductive carbon networks.[21, 22] The presence of transition metals such Cu, Zn, and Co may further improve the electrochemical performance of MOF-derived materials through synergistic interactions, enhanced conductivity, and providing a greater number of active sites.[23, 24]

However, several challenges face the adoption of pure metal chalcogenides amongst which are their poor electronic and electrical conductivity as well as the aggregation of particles which limits the full utilization of active sites.[25] Another important issue to address is stability during long cycling or under harsher conditions, as selenides and sulfides oxidize or face structural changes under oxidative potentials. Additionally, comprehensive optimization of the interface and charge transfer kinetics is crucial for both capacitive and catalytic performance.[26, 27] A number of investigations have demonstrated that the chalcogenide composites derived from MOFs can deliver excellent electrochemical energy storage and conversion performance. Guo et al.[28] have prepared Se vacancy (V_a) enabled V_a-ZnSe/$NiCoSe_2$ trimetallic selenide electrodes derived from ZIF-8@ZIF-67 core-shell MOF. The electrode exhibits a specific capacitance of 1563 F g^{-1} at 1 A g^{-1}. The asymmetric device V_a-ZnSe/$NiCoSe_2$/AC delivered an energy density of 41.9 Wh kg^{-1} at 750 W kg^{-1}. Tang et al.[29] has designed $CoSe_2$@NiOOH and $CoSe_2$@NiFeOOH catalysts derived from Co-based MOF deposited on nickel foam. The catalysts demonstrated low Tafel slopes of 199 mV dec^{-1} and 73 mV dec^{-1}, indicating superior interaction between each component of the framework. Chen et al.[30] prepared $Cu_{1.81}S$@C derived from a Cu-BTC (copper(II)-benzene-1,3,5-tricarboxylate) precursor employing a sulfurization and calcination technique. The $Cu_{1.81}S$@C was employed as an electrode material for supercapacitors and delivered a specific capacitance of 291.1 F g^{-1} at 1 A g^{-1} with a capacity retention of 83.6% at 10 A g^{-1}. Maniyazagan et al.[31] have synthesized MOF-derived S/CuCoPSe@C nanoparticles, employing 2,2-thiodiacetic acid, for water splitting. The S/CuCoPSe@C catalyst delivered an overpotential of 360 mV for OER with a Tafel slope of 116 mV dec^{-1}.These results have clearly demonstrated the excellent potential of MOF-derived metal selenides and sulfides for energy storage and water splitting applications.

View Article Online
DOI: 10.1039/D6TA01424K

In comparison to MOF-derived metal selenides, metal sulfides demonstrate superior performance overall which can be assigned to numerous synergistic effects. The sulfides exhibit higher intrinsic conductivity due to their stronger bonding and band structure. When sulfide-based heterostructures are fabricated, their intimate interfaces facilitate efficient electron transport while the lattice provides an abundance of accessible active sites. Moreover, the introduction of defects, vacancies, and strain during MOF-derived sulfidation improves the pseudocapacitive behavior and more facile insertion/removal of ions with lower structural stress.[32, 33] Additionally, their integration with hierarchical porous and nitrogen-doped porous carbon (NPC) matrices can further ensure fast ion transport, greater electrolyte access, and mechanical stability while simultaneously stabilizing the sulfide phases and maintaining the conductivity throughout the heterostructure. For OER activity, sulfide surfaces can dynamically reorganize into oxo/hydroxide species which create more active catalytic centers that support faster electron transfer with enhanced performance.[34]

In this study, we synthesized ZIF-12-derived Cu/Zn/Co@NPC, $Cu_2Se/ZnSe/CoSe_2$@NPC, and $Cu_2S/ZnS/CoS_2$@NPC heterostructures through a route involving post-synthetic Cu/Zn incorporation into a ZIF-12-based precursor, followed by pyrolysis and chalcogenization. In particular, the work provides a comparative investigation of metallic, selenide, and sulfide derivatives within the same materials platform for both supercapacitor and OER applications. Compared with previous reports, the advance here lies in the expanded heterostructure design, the direct comparison of the three derivative families, and the combined assessment of energy-storage and electrocatalytic performance within one unified ZIF-12-derived system. All the heterostructures were comprehensively characterized by structural, morphological, and spectroscopic techniques. Among all of the materials investigated, sulfide-based $Cu_2S/ZnS/CoS_2$@NPC has outperformed the selenide and metallic-based materials, demonstrating the highest specific capacitance and OER performance. This superior performance of $Cu_2S/ZnS/CoS_2$@NPC can be assigned to high conductivity, abundant redox active sites, favorable heterostructure interfaces, and a robust structure with fast ion/electron transport. The performance of a single material for energy storage and conversion not only provides a bifunctional electrode material but also offers new routes for MOF-derived, multimetal chalcogenide/NPC heterostructures. Additionally, this study highlights the multifunctionality of MOF-derived chalcogenide heterostructures with respect to their potential in integrated energy storage and conversion technologies, especially in SCs and OER catalysis applications. The rational MOF to

View Article Online
DOI: 10.1039/D6TA01424K

chalcogenide transformation provides a compositional and scalable strategy by which to engineer multimetallic heterointerfaces with high electronic conductivity and synergistic redox behavior.

Experimental Section

Materials

Benzimidazole ($C_7H_6N_2$ ≥98.0%), copper nitrate hexahydrate ($Cu(NO_3)_2.6H_2O$ ≥99.99%), zinc nitrate hexahydrate ($Zn(NO_3)_2.6H_2O$ ≥98%), cobalt (II) nitrate hexahydrate ($Co(NO_3)_2.6H_2O$ ≥98%), cetyltrimethylammonium bromide (CTAB, $CH_3(CH_2)_{15}N(Br)(CH_3)_3$ ≥98%), selenium powder (Se ≥99.99%), sulfur powder (S ≥99.8%), ammonium hydroxide (NH_4OH ≥32% NH_3 basis), methanol (CH_3OH ≥99.9%), toluene ($C_6H_5CH_3$ ≥99.8%), acetone (CH_3COCH_3 ≥99%), potassium hydroxide (KOH ≥85%), nickel foam (porosity ~ 95%), carbon black (C ≥99%), polyvinylidene fluoride (PVDF ≥99%), and N-methyl-2-pyrrolidone (NMP ≥99.7%) were purchased from Sigma-Aldrich and used as received.

Synthesis of Cu/Zn/Co@NPC

In a typical synthesis, ZIF-12 was prepared as a parent MOF precursor. Firstly, 4 mmol of benzimidazole was added in 100 mL of methanol under continuous stirring while a solution of 100 mL toluene and 4 mmol of ammonium hydroxide were added dropwise at room temperature. Then, 2 mmol of cobalt nitrate hexahydrate was added and stirred for 3 hours to ensure crystallization. The precipitates of zeolitic imidazolate framework-12 (ZIF-12) were collected by centrifugation and washed several times with methanol and dried overnight at ambient conditions. Subsequently, 2 mmol of copper nitrate hexahydrate, 2 mmol of zinc nitrate hexahydrate, and 100 mg of CTAB were dissolved in 100 mL of a methanol-toluene mixture with ratio 3:1 mol% and represents solution A. Separately, 2 mg of ZIF-12 dissolved in 50 mL of a methanol-toluene mixture to prepare solution B. Subsequently, solution A was added dropwise to solution B under continuous stirring for 3 hours, leading to the formation of light purple precipitates.[35] The resulting mixture was centrifuged, washed with methanol and dried over night at 70 °C under vacuum. Finally, the powder was calcined at 700 °C for 3 hours under an argon atmosphere which yielded a black Cu/Zn/Co@NPC powder.

Synthesis of $Cu_2Se/ZnSe/CoSe_2$@NPC and $Cu_2S/ZnS/CoS_2$@NPC

The 0.3 g of the Cu/Zn/Co@NPC precursor previously prepared was thoroughly ground with selenium or sulfur (0.3 g) powder to obtain a homogeneous mixture. The mixture was sintered at 700 °C for 2 hours under continuous argon flow by maintaining a heating rate of 5 °C min^{-1} to

View Article Online
DOI: 10.1039/D6TA01424K

reach the required temperature. This result in black pyrolyzed powders of $Cu_2Se/ZnSe/CoSe_2$@NPC and $Cu_2S/ZnS/CoS_2$@NPC which were collected. The schematic representation for the preparation of MOF-derived heterostructure is displayed in **Figure 1.**

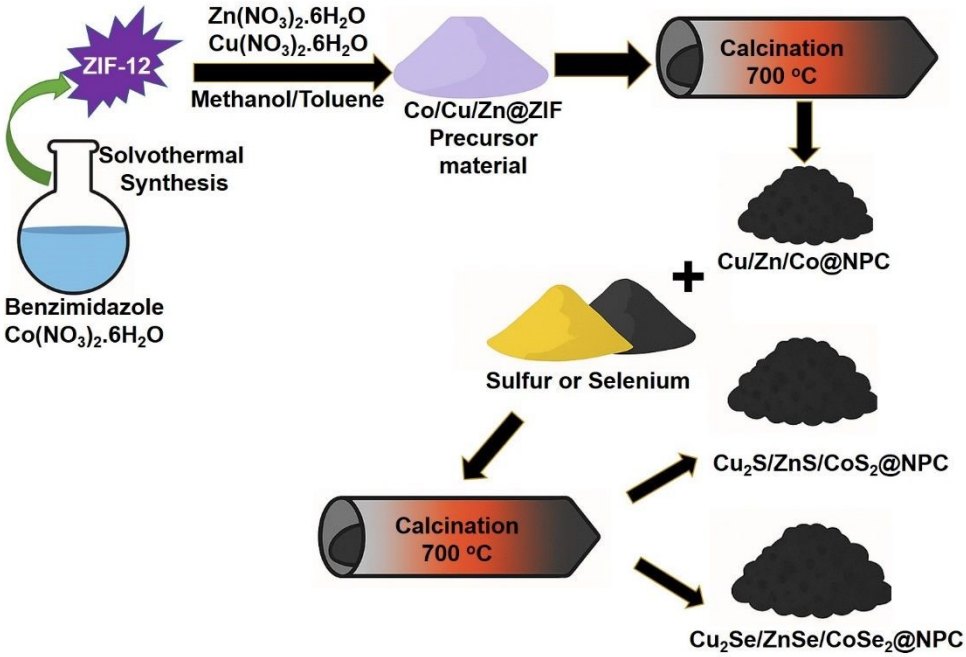

Figure 1. Schematic illustration for the synthesis of MOF-derived heterostructure materials.

Electrode Fabrication and Measurement

The synthesized MOF-derived heterostructures were used as active materials to fabricate electrodes and their electrochemical performance evaluated. The nickel foam activation process was carried out using 1 M HCl, acetone, and deionized water. A thick slurry was prepared by mixing 80 wt% active material, 10 wt% conductive carbon, and 10 wt% PVDF using NMP as solvent. The resulting homogeneous slurry was coated onto the activated nickel foam (1 cm × 1 cm) and dried at 50 °C for 12 hours. The loaded mass was approximately 1 mg ± 5% as determined from the mass difference of the substrate before and after coating. The mass loading 1 mg (±5%) is relatively low which was chosen to ensure uniform coverage and accurate electrochemical measurements while minimizing diffusion or mass transport limitations. All electrochemical measurements were performed on a Corrtest instrument (version 6.4). Asymmetric devices were fabricated employing the same method except that the dimensions of the nickel foam substrates were 1.5 cm ×1.5 cm. Specific capacitance (C_{sc}) values were evaluated from galvanostatic charge-discharge using equation 1.

View Article Online
DOI: 10.1039/D6TA01424K

$$C_{sc}=\frac{I\times\Delta t}{m\times\Delta V} \quad (1)$$

where C_{sc} is determined in F g^{-1}, I is the current in amperes (A), m the mass in grams, Δt the discharge time in seconds (s), and ΔV the potential in volt.

For electrochemical OER investigations, equations 2 and 3 have been used.

$$E_{RHE} = E_{Ag/AgCl} + (0.1976+0.059\ pH)\ V \quad (2)$$

$$\eta = E_{RHE} - 1.23\ V \quad (3)$$

Equation 2, a version of the Nernst equation, has been used to calibrate all potentials. The standard potential of the Ag/AgCl/3 M KCl (0.1976 V vs SHE) electrode was used at 25 °C with the Nernstian slope of 0.059 V adjusted for the effect of pH on the potential. All potentials reported in this study are with respect to this reference electrode. The value of 1.23 V is the minimum theoretical potential required to split water into hydrogen and oxygen under standard conditions as per equation 3. The Tafel equation (4) was employed to evaluate the kinetic parameters.

$$\eta = b\log(j) + a \quad (4)$$

where b is evaluated from the slope, j denotes the current density and a is a constant found from the intercept of the line with the y-axis.

The double layer capacitance (C_{dl}) was calculated from the CV profile in the non-Faradaic window ranging from -0.3 to -0.2 V against the Ag/AgCl reference electrode at various scan rates from 100 to 500 mV s^{-1}. The electrochemical surface area (ECSA) was then evaluated using equation 5.

$$ECSA=\frac{C_{dl}}{C_{sc}} \quad (5)$$

where C_{sc} is the specific capacitance of the materials. The turnover frequency (TOF) is calculated using equation 6.

$$TOF = \frac{j\times A}{(4\times F\times n)} \quad (6)$$

where j is the current density, A the area of electrode cm^2, F the Faraday constant (96,485 C mol^{-1}), and the factor of 4 represents the four-electron process in the OER, and n the number of moles of catalyst used during the electrolysis experiment.

Physical Characterization with Methods of Preparation

The phase purity of all materials synthesized was determined using X-ray diffraction (XRD, Rigaku Rint 2000 employing Cu Kα radiation) in the 2θ range from 10 to 80°. Raman spectra (WITec alpha300R, λ = 532 nm) were recorded to probe the internal structure of the materials. Scanning electron microscopy (SEM, Zeiss Sigma 300) was utilized to analyze the surface

View Article Online
DOI: 10.1039/D6TA01424K

morphology and transmission electron microscopy (TEM) (Hitachi HT7700). Energy dispersive X-ray (EDX) spectroscopy was employed to probe the elemental composition and homogeneous distribution via elemental mapping. The N_2 adsorption-desorption isotherms were recorded using a Micromeritics 3Flex Gas Adsorption system (version 5.00). X-ray photoelectron spectroscopy (XPS) analysis was performed on a Thermo Scientific K-Alpha spectrometer.

Results and discussion

The phase purity of MOF-derived Cu/Zn/Co@NPC, Cu_2Se/ZnSe/$CoSe_2$@NPC, and Cu_2S/ZnS/CoS_2@NPC heterostructures were confirmed via X-ray diffraction (XRD) as shown in **Figure 2(a)**. The Cu/Zn/Co@NPC displayed diffraction peaks at 43.3°, 50.4°, and 74.1° which can be assigned to face-centered cubic Cu (ICDD: 71-4610)[36] while the peaks that appear at 65.4° and 36.3° are due to metallic Zn (ICDD: 04-0831)[37] and Co (ICDD: 15-0806)[38] phases. The existence of metallic peaks confirmed the complete reduction of metal ions during the pyrolysis process under the Ar atmosphere. The Cu_2Se/ZnSe/$CoSe_2$@NPC sample demonstrates peaks at 27.3°, 33.5°, 36.0°, 44.5°, 45.4°, 51.5°, 52.6°, 53.8°, 56.3°, 64.4°, and 76.6° which correspond to Cu_2Se (ICDD: 06-0680),[39] ZnSe (ICDD: 065-9602),[40] and $CoSe_2$(ICDD: 53-0449)[41]. The presence of these different phases in the sample indicates a successful anion exchange and the selenization of metals within the porous carbon framework. However, the Cu_2S/ZnS/CoS_2@NPC heterostructure exhibits peaks at 26.5°, 28.5°, 31.2°, 32.7°, 37.9°, 47.6°, 49.9°, 54.7°, 56.4°, and 76.9° which correspond to Cu_2S (ICDD: 89-2531),[42] ZnS (ICDD: 03-065-5476),[43] and CoS_2 (ICDD: 41-1471)[44]. The confirmation of the presence of all three sulfides without the presence of any impurity peaks suggests the success of the sulfidation process in which the metal precursors have fully converted to their corresponding sulfides. The XRD pattern confirms the complete structural transformation of the materials, all of which were derived from ZIF-12, as can be seen in **Figure S1**.

The structural features of the MOF-derived Cu/Zn/Co@NPC, Cu_2Se/ZnSe/$CoSe_2$@NPC, and Cu_2S/ZnS/CoS_2@NPC heterostructures were elucidated via Raman analysis and which was used to confirm the carbon matrix and metal-chalcogen vibrational modes as displayed in **Figure 2(b)**. The Cu/Zn/Co@NPC exhibits distinct bands at 1376 and 1562 cm^{-1} which correspond to the D and G bands, respectively. The G band is present due to the E_2g in-plan stretching mode of sp^2-bonded graphitic carbon while the D band is assigned to the defect-activated mode of six-membered sp^2 rings which are Raman-active only in the presence of structural disorder or finite

View Article Online
DOI: 10.1039/D6TA01424K

crystallite size. The band that appears at 2892 cm^{-1} due to the second-order 2D (or G‘) mode, indicates the partial graphitization of the NPC matrix. The $Cu_2Se/ZnSe/CoSe_2$@NPC possesses bands at 1349, 1583, and 2905 cm^{-1} which are characteristics of the D, G, and 2D modes of graphitic NPC with minor redshifts which is an indication of electronic coupling between selenides and carbon. While $Cu_2S/ZnS/CoS_2$@NPC showed bands at 1369, 1576, and 2919 cm^{-1} attributed to D, G, and 2D modes along with very low intensity bands at 165, 319, and ~695 cm^{-1} due to low-frequency lattice vibrational modes of metal-S bonding, all displayed a slight shift which confirmed the enhanced graphitization and strong interaction between sulfide and NPC framework. On the other hand, intensity ratios (I_D/I_G) evaluated from the Raman spectra are 0.88, 0.85, and 0.86 for MOF-derived Cu/Zn/Co@NPC, $Cu_2Se/ZnSe/CoSe_2$@NPC, and $Cu_2S/ZnS/CoS_2$@NPC heterostructures, indicating comparable degrees of structural disorder within the carbon matrices of all samples. The intensity ratio values confirmed the presence of a partially ordered NPC matrix, which has a substantial population of defects and edge sites, rather than full graphitic or amorphous carbon. The higher value of I_D/I_G for Cu/Zn/Co@NPC suggests a greater defect density, arising from metal induced disruption in the NPC network during pyrolysis, while lower I_D/I_G values for $Cu_2Se/ZnSe/CoSe_2$@NPC, and $Cu_2S/ZnS/CoS_2$@NPC indicates improved local graphitization.[45] These observations confirmed the successful formation of a conductive NPC framework with an embedded multimetallic chalcogenide phase.

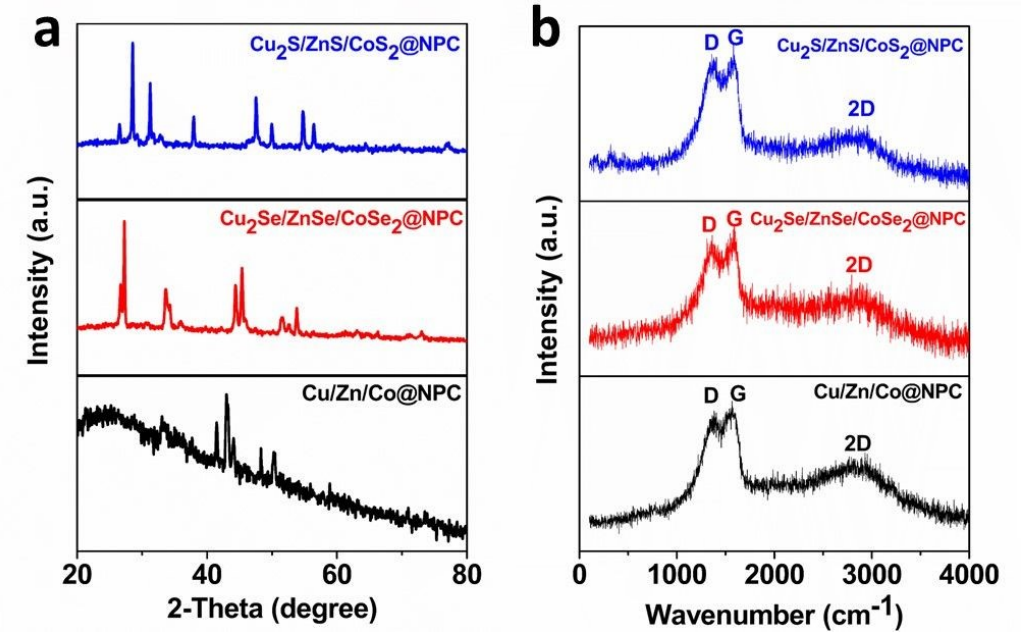

View Article Online
DOI: 10.1039/D6TA01424K

Figure 2. Structural analysis: a) XRD patterns of Cu/Zn/Co@NPC (black line), $Cu_2Se/ZnSe/CoSe_2$@NPC (red line), and $Cu_2S/ZnS/CoS_2$@NPC (blue line), b) Raman spectra of Cu/Zn/Co@NPC (black line), $Cu_2Se/ZnSe/CoSe_2$@NPC (red line), and $Cu_2S/ZnS/CoS_2$@NPC (blue line).

SEM imaging revealed the surface morphology and microstructural features of MOF-derived Cu/Zn/Co@NPC, $Cu_2Se/ZnSe/CoSe_2$@NPC, and $Cu_2S/ZnS/CoS_2$@NPC heterostructures. The images of pristine Cu/Zn/Co@NPC at different magnifications exhibit an irregular morphology along with interconnected nanoclusters and show excellent preservation of the MOF-derived framework obtained by pyrolysis under an inert atmosphere, as seen in **Figure 3(a, b, c)**. The presence of an interconnected network and porous texture improves access to the surface-active sites and supports the efficient diffusion of ions during electrochemical measurements. Additionally, the elemental composition and purity of the MOF-derived Cu/Zn/Co@NPC, $Cu_2Se/ZnSe/CoSe_2$@NPC, and $Cu_2S/ZnS/CoS_2$@NPC heterostructures was confirmed via energy dispersive X-ray (EDX) spectra as shown in **Figure S2(a, b, c)**. Furthermore, TEM micrographs were recorded of MOF-derived Cu/Zn/Co@NPC, $Cu_2Se/ZnSe/CoSe_2$@NPC, and $Cu_2S/ZnS/CoS_2$@NPC heterostructures as presented in the **Figure 3(d, e, f)**. The images showed that the materials exhibited irregular shaped with aggregated nanostructure. While micrographs have dense contrast particles, confirming the successful conversion of MOF-precursors into metal chalcogenides phases with more crystallinity. The presence of bulk/cluster like morphology indicates that the MOF templates driven the structural evolution, resulting to porous nanograins. The interconnected frameworks in some regions also attributes to the collapse of organic ligands when selenization/sulfidation occur, produce conductive chalcogenides networks. Additionally, high-resolution TEM (HRTEM) images demonstrate clear lattice fringes, confirming the crystalline nature of the MOF-derived chalcogenides as shown in **Figure 3(g, h, i)**. The interplanar lattice d-spacing calculated for Cu/Zn/Co@NPC, $Cu_2Se/ZnSe/CoSe_2$@NPC, and $Cu_2S/ZnS/CoS_2$@NPC heterostructures are 0.188 nm, 0.46 nm, and 0.34 nm, respectively. The different values of d-spacing reveal the coexistence of multiple crystallographic planes/phases. Thus, this type of structural heterogeneity can produce huge active sites and support the charge transport process.

View Article Online
DOI: 10.1039/D6TA01424K

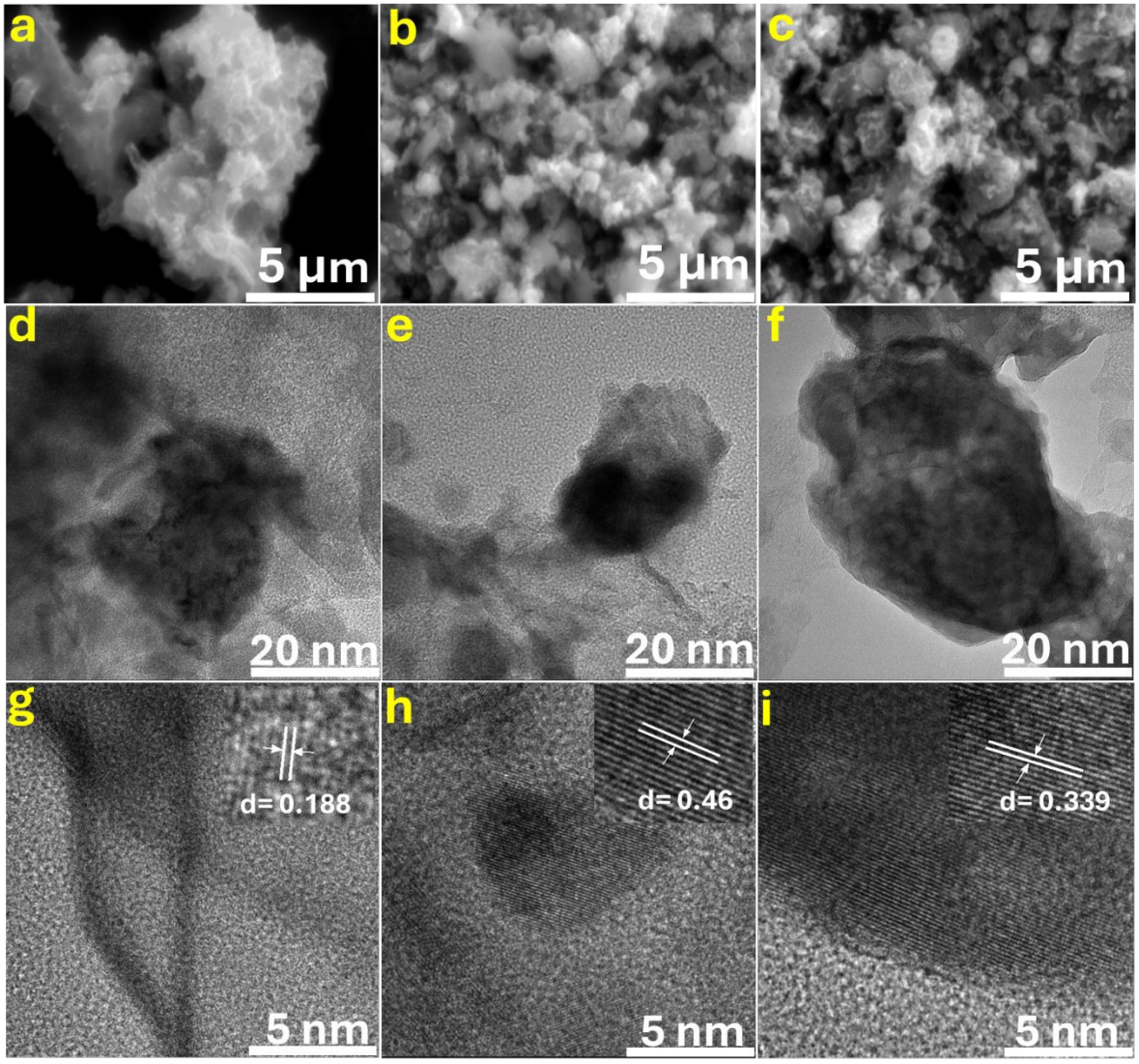

Figure 3. Top row: SEM images of a) Cu/Zn/Co@NPC, b) $Cu_2Se/ZnSe/CoSe_2$@NPC,and c) $Cu_2S/ZnS/CoS_2$@NPC heterostructures, Middle row: TEM images of d) Cu/Zn/Co@NPC, e) $Cu_2Se/ZnSe/CoSe_2$@NPC,and f) $Cu_2S/ZnS/CoS_2$@NPC heterostructures, Bottom row: HRTEM images of g) Cu/Zn/Co@NPC, h) $Cu_2Se/ZnSe/CoSe_2$@NPC,and i) $Cu_2S/ZnS/CoS_2$@NPC heterostructures.

Brunauer–Emmett–Teller (BET) analysis was employed to examine the porosity of the MOF-derived Cu/Zn/Co@NPC, $Cu_2Se/ZnSe/CoSe_2$@NPC, and $Cu_2S/ZnS/CoS_2$@NPC heterostructures through nitrogen adsorption-desorption as shown in **Figure 4(a, b, c)**. The synthesized materials exhibit typical type-II isotherm curves by a type H3 hysteresis loop which attests to the fact that the mesoporous materials are composed of aggregated structures rather than possess true MOF-type microporosity. At low relative pressures, the profile of a Type II adsorption isotherm sharply increases, indicating the filling of small pores. As the pressure increases, the monolayer adsorption

View Article Online
DOI: 10.1039/D6TA01424K

translates to multilayer adsorption and, due to the presence of a well-developed mesopore structure, the adsorbance sharply rises when the P/P_0 value is close to 1. The surface areas determined for the Cu/Zn/Co@NPC, $Cu_2Se/ZnSe/CoSe_2$@NPC, and $Cu_2S/ZnS/CoS_2$@NPC heterostructures are 35.36, 19.16, and 115.37 $m^2\ g^{-1}$, respectively. Additionally, Barrett-Joyner-Halenda (BJH) plots demonstrate that all the materials under study possess a highly porous architecture indicative of a mesoporous structure as presented in **Figure 4(d, e, f)**. These properties indicate the potential of the synthesized materials for charge storage and conversion applications.

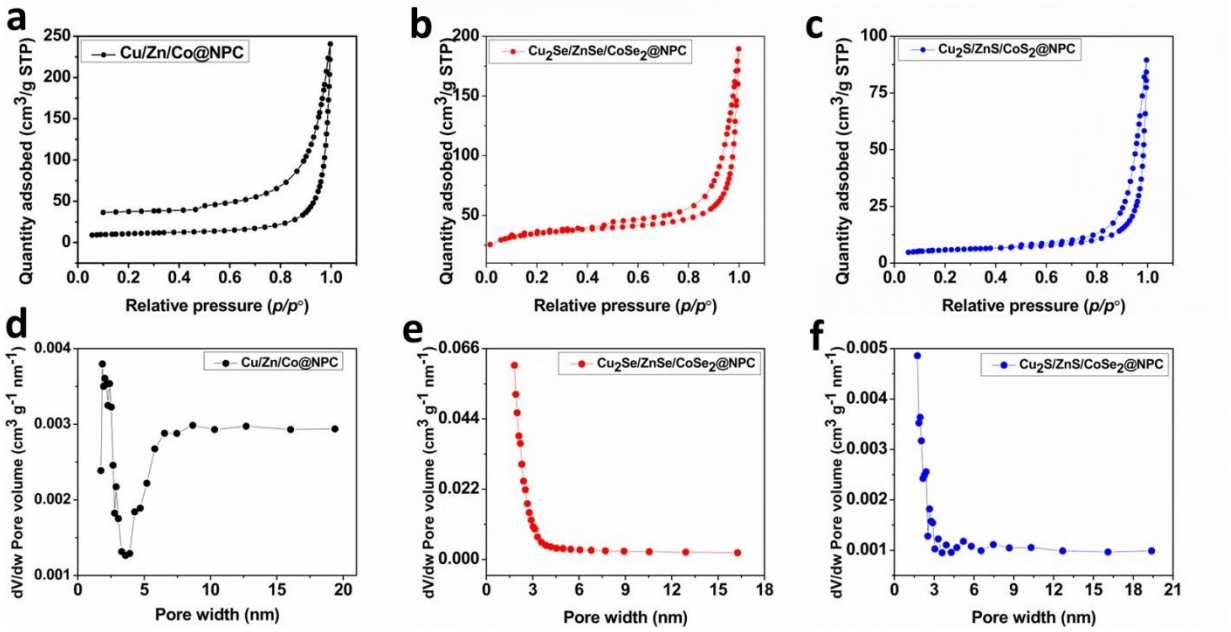

Figure 4. Nitrogen adsorption-desorption isotherm for: a) Cu/Zn/Co@NPC, b) $Cu_2Se/ZnSe/CoSe_2$@NPC, and c) $Cu_2S/ZnS/CoS_2$@NPC heterostructures, BJH pore size distribution curves for: d) Cu/Zn/Co@NPC, e) $Cu_2Se/ZnSe/CoSe_2$@NPC, and f) $Cu_2S/ZnS/CoS_2$@NPC heterostructures.

The oxidation state and surface functional groups of the MOF-derived $Cu_2S/ZnS/CoS_2$@NPC heterostructure were evaluated employing XPS analysis. The survey spectrum validated the presence of Cu, Zn, Co, S, N, and C in the sample as shown in **Figure S3**. The Cu 2p high-resolution bands that appear at 934.3 and 954.1 eV are assigned to $Cu^{2+}\ 2p_{3/2}$ and $Cu^{2+}\ 2p_{1/2}$ with the existence of two satellite bands at 942.2 and 962.5 eV, as displayed in **Figure 5(a)**.[46] The Zn 2p demonstrates a doublet of bands at 1021.8 and 1044.6 eV which are consistent with $Zn^{2+}\ 2p_{3/2}$ and $Zn^{2+}\ 2p_{1/2}$ in ZnS, as depicted in **Figure 5(b)**.[47] Similarly, Co 2p exhibits bands at 782.2 and 798.7 eV which correspond to $Co^{3+}\ 2p_{3/2}$ and $Co^{3+}\ 2p_{1/2}$ with the presence of two satellite peaks at 785.1 and 802.6 eV assigned to $Co^{2+}\ 2p_{3/2}$ and $Co^{2+}\ 2p_{1/2}$, respectively, as seen in **Figure 5(c)**.[48]

View Article Online
DOI: 10.1039/D6TA01424K

S 2p has deconvoluted into a S $2p_{3/2}$ and S $2p_{1/2}$ doublet, centered at 163.7 and 168.5 eV, which are assigned to sulfide ions from the metal sulfides as in **Figure 5(d)**.[49] The N 1s spectrum exhibits three bands at 398.3, 400.6, and 403.2 eV which correspond to pyridinic-N, pyrrolic-N, and graphitic-N, respectively, as displayed in **Figure 5(e)**. The presence of pyridinic and graphitic N confirmed the successful N-doping into the porous carbon matrix which is derived from the MOF precursors. The presence of N-species tunes the electronic coupling, conductivity, and anchoring sites for metal sulfide materials. The C 1s spectrum shows 2 bands at 284.5 and 286.3 eV which are attributed to C-C/graphitic carbon and metal-O-C species as shown in **Figure 5(f)**.[50] The XPS spectra of MOF-derived Cu/Zn/Co@NPC and $Cu_2Se/ZnSe/CoSe_2$@NPC heterostructures with corresponding binding energy values for each element are presented in **Figure (S4 & S5)**.

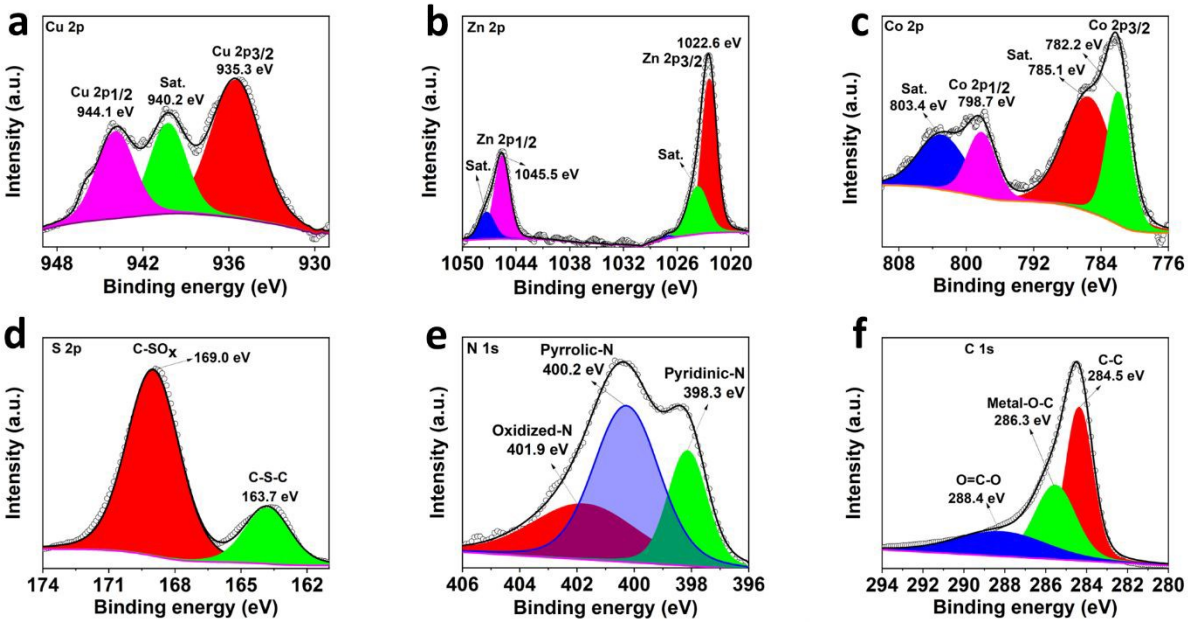

Figure 5. XPS analysis of MOF-derived $Cu_2S/ZnS/CoS_2$@NPC heterostructure: a) Cu 2p, b) Zn 2p, c) Co 2p, d) S 2p, e) N 1s, and f) C 1s.

Electrochemical Measurements

Electrolyte optimization was carried out, using $Cu_2S/ZnS/CoS_2$@NPC as the active electrode material, in 2 M NaOH and 2 M KOH as presented in **Figure S6(a)**. The cyclic voltammetry (CV) curves show more prominent redox peaks and increased area under the curve in 2 M KOH electrolytes indicating KOH to be the electrolyte of choice for further investigations. It is well reported that K^+ ions possess smaller hydrated ionic radii of 3.31 Å and as such exhibit lower solution resistance than Na^+ ions which possess larger hydrated ionic radii of 3.82 Å.[51] It was observed that the $Cu_2S/ZnS/CoS_2$@NPC electrode possessed the highest capacitance compared to

View Article Online
DOI: 10.1039/D6TA01424K

that of electrodes fabricated from the other materials when measured in KOH electrolyte. The electrochemical performance of electrodes fabricated using MOF-derived Cu/Zn/Co@NPC, $Cu_2Se/ZnSe/CoSe_2$@NPC, and $Cu_2S/ZnS/CoS_2$@NPC materials was evaluated via CV in a potential window of -0.2 to 0.6 V in 2 M KOH electrolyte. Comparative CV profiles of all materials conducted at 10 mV s^{-1}, along with that of the bare nickel foam, are presented in **Figure S6(b).** The values calculated for the areas under the CV profiles for bare nickel foam and MOF-derived Cu/Zn/Co@NPC, $Cu_2Se/ZnSe/CoSe_2$@NPC, and $Cu_2S/ZnS/CoS_2$@NPC are 0.00183, 0.01250, 0.01801, and 0.03511 A V, respectively. The greater area under the CV profile of the $Cu_2S/ZnS/CoS_2$@NPC heterostructure confirmed its higher energy storage capacity and rate capability. To further investigate the effect of scan rate on all three MOF-derived materials, CV profiles were conducted in range from 10 to 100 mV s^{-1}, as presented in **Figure 6(a, b, c)**. The CV profiles demonstrate the prominent redox peaks which are associated with the Faradaic reactions that occur at the electrode-electrolyte interface due to reversible redox chemistry, i.e. oxidation and reduction of the metal centers present in the materials. The consistent nature of the curves with increasing scan rate is attributed to the excellent stability of the fabricated electrodes possessing fast electron transfer and ion transportation and which is indicative of the battery-type behavior of the materials. A very minute change in the redox peak positions was observed, which can be accounted for by the reversibility and excellent stability of the electrode materials. The plausible mechanisms for the redox reactions[52-54] are represented by equations 7, 8, and 9, 10, 11, 12, respectively.

$$Cu_2S+OH^- \rightleftharpoons Cu_2SOH+e^- \quad (7)$$

$$Cu_2SOH+OH^- \rightleftharpoons Cu_2SO+H_2O+e^- \quad (8)$$

$$ZnS+OH^- \rightleftharpoons ZnSOH+e^- \quad (9)$$

$$ZnSOH+OH^- \rightleftharpoons ZnSO+H_2O+e^- \quad (10)$$

$$CoS_2+OH^- \rightleftharpoons CoS_2OH+e^- \quad (11)$$

$$CoS_2OH+OH^- \rightleftharpoons CoS_2O+H_2O+e^- \quad (12)$$

Galvanostatic charge-discharge (GCD) profiles of all fabricated electrodes were obtained with each demonstrating non-linear curves, which is again indicative of the battery-type behavior of these materials[55], see **Figure 6(d, e, f)**. The specific capacitance values calculated for MOF-derived Cu/Zn/Co@NPC, $Cu_2Se/ZnSe/CoSe_2$@NPC, and $Cu_2S/ZnS/CoS_2$@NPC heterostructures are 620 F g^{-1}, 894 F g^{-1}, and 1206 F g^{-1} at 1 A g^{-1} while 411 F g^{-1}, 154 F g^{-1}, and 520 F g^{-1} at 10 A

View Article Online
DOI: 10.1039/D6TA01424K

g^{-1}, respectively. The excellent electrochemical energy storage performance of the MOF-derived Cu/Zn/Co@NPC heterostructure, $Cu_2Se/ZnSe/CoSe_2$@NPC heterostructure, and $Cu_2S/ZnS/CoS_2$@NPC heterostructure can be attributed to their unique heterostructure architecture and MOF-derived porous carbon framework. The presence of multiple transition metals (Cu, Zn, and Co) provides abundant redox-active sites, which facilitate fast Faradaic reactions during charge-discharge processes. The formation of selenide and sulfide phases improves electrical conductivity and enhances charge transfer compared to oxide counterparts. In addition, the NPC matrix derived from the MOF template offers a high surface area, interconnected porous channels, and improved electrical conductivity, which promotes efficient electrolyte ion diffusion and electron transport. Furthermore, the synergistic interaction between the metal chalcogenides and conductive carbon network helps stabilize the active sites and accommodates volume variations during cycling, leading to improved capacitance, rate capability, and long-term electrochemical stability of the electrodes. The highest specific capacitance, exhibited by $Cu_2S/ZnS/CoS_2$@NPC, is attributed to facile transport of electron/ions at the electrode-electrolyte interface due to superior conductivity, abundant redox active sites, favorable heterostructure interfaces, and robust microstructure compared to the Cu/Zn/Co@NPC and $Cu_2Se/ZnSe/CoSe_2$@NPC materials. Even at higher current density, $Cu_2S/ZnS/CoS_2$@NPC demonstrates an appreciable value of specific capacitance as presented on **Table 1**. The $Cu_2Se/ZnSe/CoSe_2$@NPC exhibits a large drop in specific capacitance from 894 F g^{-1} at 1 A g^{-1} to 154 F g^{-1} at 10 A g^{-1} because selenide electrodes may have slower ion diffusion and limited electronic conductivity. At high current densities, diffusion limitations dominate, preventing full utilization of active sites, whereas $Cu_2S/ZnS/CoS_2$@NPC and Cu/Zn/Co@NPC retain higher capacitance due to more efficient ionic and electronic transport or a more porous architecture. This behavior is consistent with battery-type materials, where kinetically slow Faradaic processes cannot keep up under fast charging conditions. Additionally, this exceptional performance of MOF-derived $Cu_2S/ZnS/CoS_2$@NPC makes it a promising electrode material compared with both the MOF-derived pristine multimetal and selenide-based materials. Moreover, different working potential windows were employed in the CV and GCD studies to avoid water catalysis reactions during the charging process.[56]

Electrochemical impedance spectroscopy (EIS) was carried out at open circuit potential (OCP) to investigate the charge transfer dynamics of all fabricated electrodes. The Nyquist plots have a very

View Article Online
DOI: 10.1039/D6TA01424K

small semicircle in the low frequency region with steep linear portions in the higher frequency regions as shown in **Figure 6(g)**. The depressed semicircle in the high-frequency region indicates non-ideal charge transfer and surface heterogeneity, represented by a constant phase element (CPE). The low-frequency line with an angle less than 90° suggests diffusion-controlled ion transport (Warburg impedance) rather than ideal capacitive behavior. This confirms a mixed charge-storage mechanism involving both pseudocapacitive surface reactions and diffusion-controlled Faradaic processes.[8] The MOF-derived $Cu_2S/ZnS/CoS_2$@NPC heterostructure exhibits a smaller charge transfer resistance (R_{ct}) than the other heterostructures which again indicates fast electron/ion transport at the electrode-electrolyte interface. The calculated R_{ct} values for the MOF-derived Cu/Zn/Co@NPC, $Cu_2Se/ZnSe/CoSe_2$@NPC, and $Cu_2S/ZnS/CoS_2$@NPC heterostructures are 0.291 Ω, 1.197 Ω, and 0.175 Ω while solution resistances (R_s) are 1.719 Ω, 0.755 Ω, and 0.456 Ω, respectively. The R_s, which is a combination of electrolyte, contact, and internal resistances, is determined from the x-axis intercept of the EIS plots. The lower R_{ct} values for $Cu_2S/ZnS/CoS_2$@NPC are assigned to the high conductivity and fast kinetics of the heterostructure. The specific capacitance values were observed to decrease with increasing current density for all of the fabricated electrodes as shown in **Figure 6(h)**. Ragone plots have been generated between specific energy densities and specific power densities for all fabricated electrodes at various current densities as presented in **Figure 6(i).** The non-linear GCD profiles indeed indicate Faradaic redox reactions rather than ideal electric double-layer capacitive (EDLC) behavior. Therefore, the material does not behave as a purely EDLC supercapacitor but rather falls into the category of battery-type or Faradaic pseudocapacitive materials. The presence of distinct redox plateaus suggests diffusion-influenced charge storage associated with reversible transition metal redox couples, which is characteristic of battery-type electrodes. This classification directly influences Ragone plot interpretation. Battery-type materials generally deliver higher specific energy due to bulk Faradaic reactions but at comparatively lower power density because ion diffusion limits fast charge-discharge. In contrast, ideal capacitors occupy the high-power density and low-energy region. Therefore, our material is expected to shift toward higher energy density while maintaining moderate power density, positioning it between conventional supercapacitors and batteries in the Ragone plot. The $Cu_2S/ZnS/CoS_2$@NPC has a much higher specific energy density at lower specific power density than the other prepared materials which indicates its potential as a more energy efficient storage material.

View Article Online
DOI: 10.1039/D6TA01424K

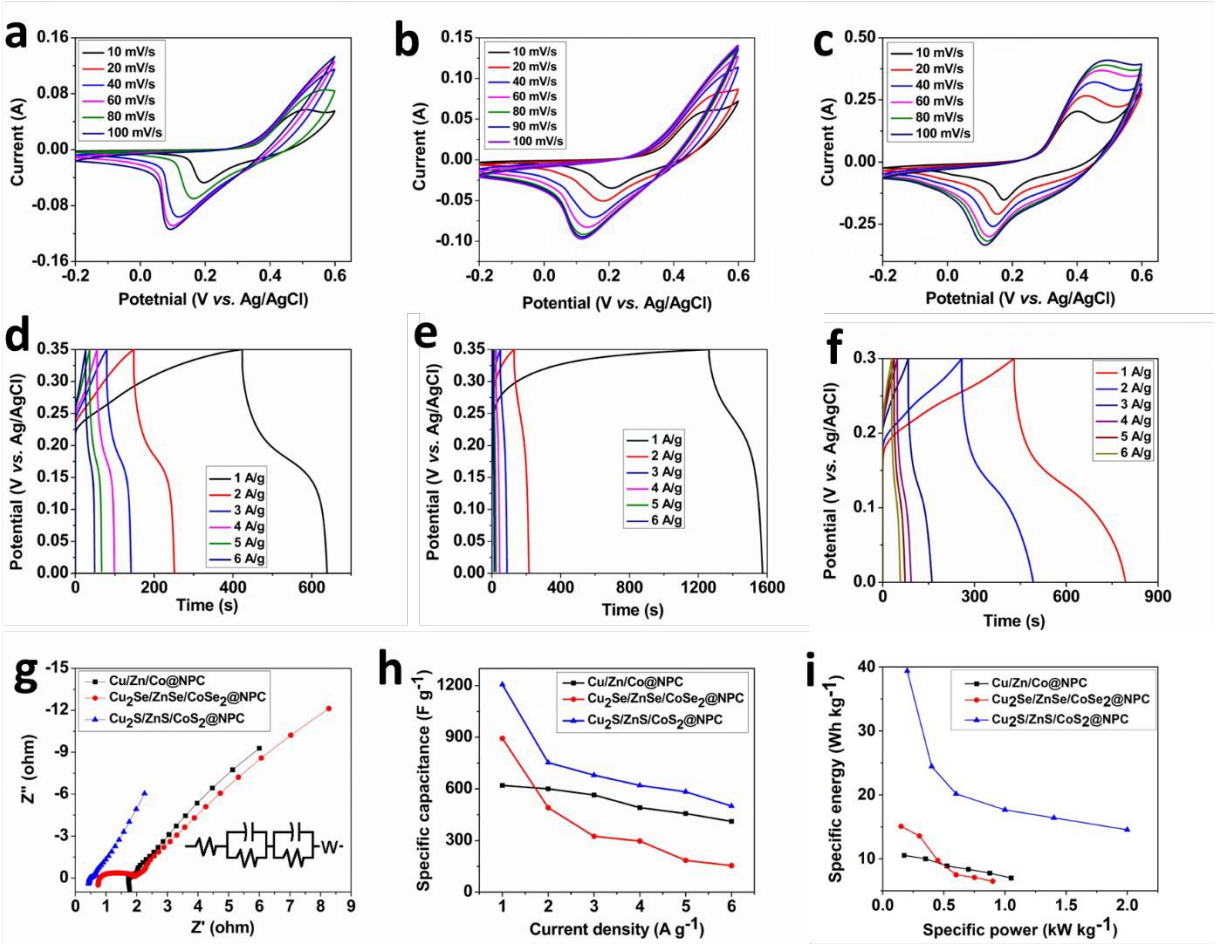

Figure 6. CV profiles at various scan rates for the: a) Cu/Zn/Co@NPC, b) $Cu_2Se/ZnSe/CoSe_2$@NPC, c) $Cu_2S/ZnS/CoS_2$@NPC heterostructures, GCD profiles for the: d) Cu/Zn/Co@NPC, e) $Cu_2Se/ZnSe/CoSe_2$@NPC, f) $Cu_2S/ZnS/CoS_2$@NPC heterostructures, g) EIS profiles, h) Current density vs. specific capacitance, and i) Ragone plots of the synthesized heterostructures.

View Article Online
DOI: 10.1039/D6TA01424K

Table 1. Specific capacitance (F g^{-1}) for all three electrode materials at different current densities.

Current density (A g^{-1})	**1**	**2**	**3**	**5**	**7**	**10**
Cu/Zn/Co@NPC,	620	600	565	491	457	411
$Cu_2Se/ZnSe/CoSe_2$@NPC	894	491	325	297	185	154
$Cu_2S/ZnS/CoS_2$@NPC	1206	753	680	620	566	520

The charge stored in the electrode is a combination of diffusion and capacitive phenomena. Therefore, it is important to evaluate the individual contributions to the overall capacity of the electrode materials. The relation between current (i) and scan rate (v) is given by the power law (equation 13).

$$i=av^b \qquad (13)$$

The value of b is evaluated from the slope of log(i) vs. log(v) and is indicative of charge storage phenomenon. Values of b in and around unity indicate capacitive storage due to the adsorption/desorption of electrolyte ions while values of b of 0.5 or below are indicative of diffusion-controlled process. The value of b calculated for $Cu_2S/ZnS/CoS_2$@NPC is 0.31 indicating diffusion-control, see **Figure 7(a)**.

Furthermore, Dunn's method has been applied to evaluate the quantitative contributions from surface and diffusion capacitances for all MOF-derived materials using equation 14.[57]

$$i(V)=k_1\upsilon+k_2\upsilon^{\frac{1}{2}} \qquad (14)$$

The values of $k_1\upsilon$ and $k_2\upsilon^{1/2}$ provide the surface and diffusion capacitances with k_1 and k_2 being determined from the slope and intercept of a plot of $i(V)/\upsilon^{½}$ vs. $\upsilon^{½}$ at a set value of the potential with associated different currents as determined from the CV profiles as shown in **Figure 7(b)**. The capacitive (pink region) and diffusion-controlled (green), indicated by the CV recorded at 10 mV s^{-1} for $Cu_2S/ZnS/CoS_2$@NPC, the calculated values of which were 13% and 87%, is presented in **Figure 7(c)**. The bar plot for surface and diffusion capacitances at various scan rates is presented in **Figure 7(d)**. As the bar plot indicates at lower scan rates the contribution from diffusion processes is higher than that of surface processes for the MOF-derived $Cu_2S/ZnS/CoS_2$@NPC material, which indicates that ions have sufficient time to permeate into the inner regions of the electrode. The implementation of similar electrode fabrication methods and the presence of analogous CV features can account for the comparable surface and diffusion-controlled contributions for all materials under study. The data for the application of Dunn's method to the

View Article Online
DOI: 10.1039/D6TA01424K

MOF-derived Cu/Zn/Co@NPC and $Cu_2Se/ZnSe/CoSe_2$@NPC materials is presented in **Figure (S7 & S8),** respectively.

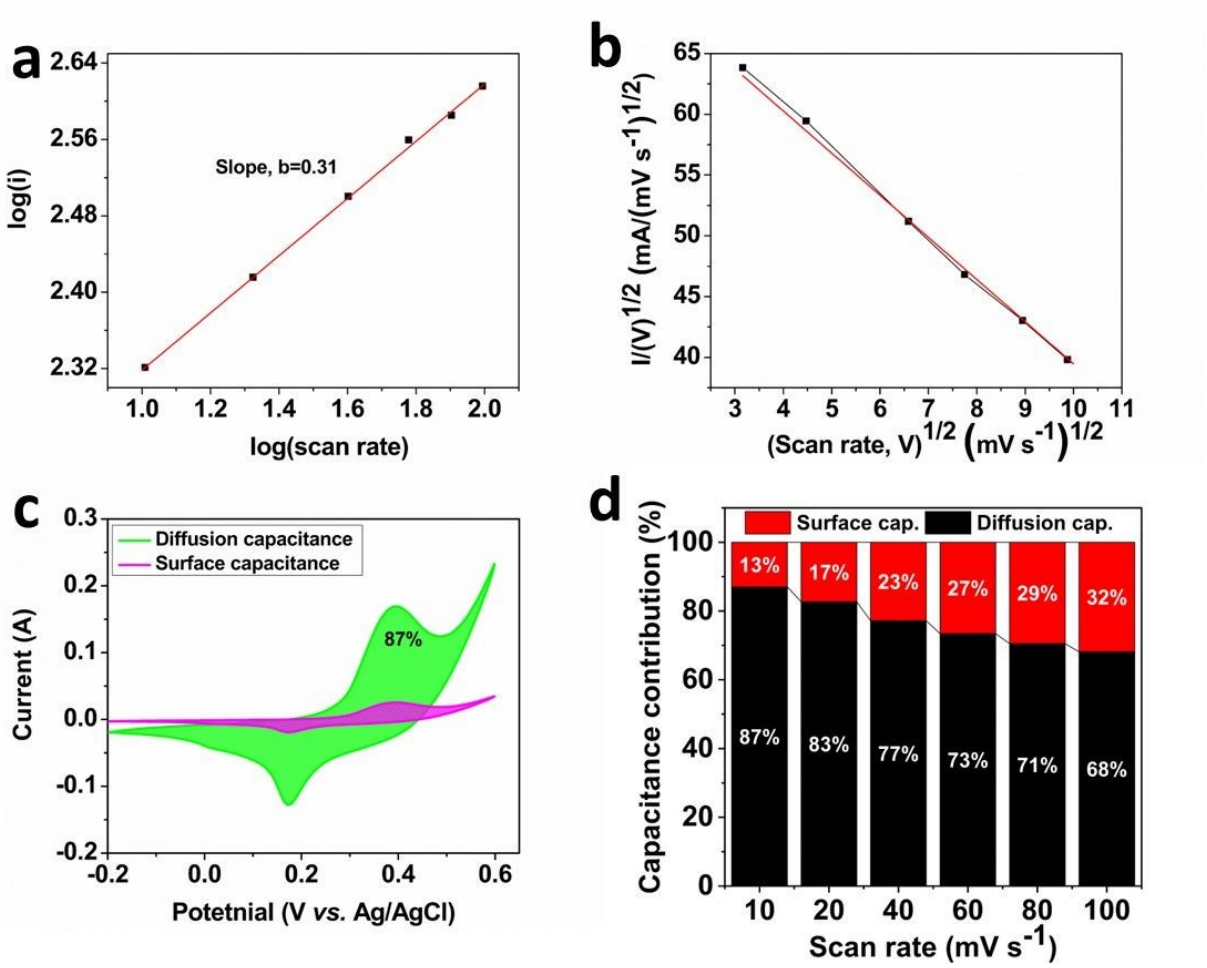

Figure 7. Dunn's method for quantitative analysis of the surface and diffusion capacitances of $Cu_2S/ZnS/CoS_2$@NPC: a) Plots of log(i) vs. log(v), b) Plots of $(i/v^{1/2})$ vs. $(v^{1/2})$, c) Contribution from surface and diffusion capacitance at 10 mV s^{-1}, d) Bar plots representing the contributions from the surface and diffusion capacitances at different scan rates.

Electrochemical Investigation of an $Cu_2S/ZnS/CoS_2$@NPC Asymmetric Device

An asymmetric device, employing the MOF-derived $Cu_2S/ZnS/CoS_2$@NPC material as the cathode and activated carbon (AC) as the anode, was fabricated. The aim of designing asymmetric devices is to take advantage of the storage capacities of two different electrode materials. The $Cu_2S/ZnS/CoS_2$@NPC electrode material provides a greater contribution to energy storage due to reversible, facile Faradaic reactions while AC stores energy via electrostatic charge accumulation and has a higher power output and long cycle life. Therefore, asymmetric devices exhibit a trade-

View Article Online
DOI: 10.1039/D6TA01424K

off with respect to energy and power density by capitalizing on the limitations of symmetric supercapacitors. Symmetric supercapacitors are quite often constrained by a narrow operating potential window and lower energy densities. AC has a significantly lower specific capacitance and cannot store an equal amount of charge as that of the MOF-derived $Cu_2S/ZnS/CoS_2$@NPC material. Therefore, the masses of active materials must be balanced on both the positive and negative electrode in order to maximize the specific capacitance of the electrode. The exact mass balance values were calculated using equation 15.

$$\frac{m_+}{m_-} = \frac{C_- \Delta V_-}{C_+ \Delta V_+} \qquad (15)$$

In accordance with the calculated values 1 mg of MOF-derived $Cu_2S/ZnS/CoS_2$@NPC and 1.5 mg of AC were coated on separate 1.5 cm × 1.5 cm activated nickel foam substrates which were employed as positive and negative electrodes, respectively. A graphical representation of the fabricated asymmetric device is presented in **Figure 8(a)**. The fabricated asymmetric device was systematically optimized across various potential window ranges from 0 V to 0.8, 1, 1.2, and 1.4 V to determine the potential range across which the complete utilization of active material and AC could be accomplished, as shown in **Figure S9**. It can be seen that beyond 1 V a distortion was observed in the behavior of the CV profiles indicative of water splitting. Therefore, in order to evaluate the asymmetric device performance, a potential window of 0 to 1 V was selected. The CV profiles were therefore recorded within this potential window in 2 M KOH electrolyte at different scan rates ranging from 10 to 100 mV s^{-1}, see **Figure 8(b)**. The GCD profiles display a rectangular shape suggesting excellent reversibility of the fabricated devices as can be seen from **Figure 8(c)**. The evaluated specific capacitance values are 114, 92, 80, 66, and 54 F g^{-1} at current densities of 3, 4, 5, 6, and 7 A g^{-1}, respectively. A Ragone plot was plotted to evaluate the energy and power density values and is presented in **Figure 8(d)**. The MOF-derived $Cu_2S/ZnS/CoS_2$@NPC material delivered an energy density of 15.83 Wh kg^{-1} at a power density of 1.5 kW kg^{-1} calculated at 3 A g^{-1}. The asymmetric device was tested for long term cycle stability and possessed a capacity retention of 92.1% over 6000 cycles as shown in **Figure 8(e)**. Nyquist plot of the asymmetric device together with the fitted equivalent circuit model is shown in **Figure 8(f)**. Nyquist plots were recorded from 0.1 Hz to 100 kHz at open circuit voltage (OCP). The black squares represent the experimental EIS data, while the red circles correspond to the fitted curve obtained from the equivalent circuit model indicating good agreement between the experimental results and the simulated data. In the high-frequency region, a small semicircle is observed, which

View Article Online
DOI: 10.1039/D6TA01424K

corresponds to the R_{ct} and interfacial processes at the electrode/electrolyte interface. In the low-frequency region, the plot shows a nearly linear behavior associated with ion diffusion and capacitive characteristics of the device. The inset zoom-in plot clearly highlights the semicircle in the high-frequency region and confirms the accuracy of the circuit fitting to the experimental Nyquist data. The R_{ct} and R_s values calculated for the MOF-derived $Cu_2S/ZnS/CoS_2$@NPC are 66.59 Ω and 2.373 Ω, respectively. These low resistance values indicate the fast kinetics of the fabricated asymmetric device based on MOF-derived $Cu_2S/ZnS/CoS_2$@NPC material. All the fitted parameters with errors have been presented in **Table S1**. Moreover, post-electrochemical characterizations were carried of assembled ASC device. The SEM images indicate that the active material is uniformly intercom on nickel foam while maintaining structural integrity without detachment as shown in **Figure S10(a, b)**. EDX spectrum confirms the presence of Cu, Zn, Co, Ni, S, C, N, and K as in **Figure S10(c)** . The Ni is due to nickel foam while K is assigned to electrolyte residues after electrochemical measurements. Also, the mapping images of each element confirm the homogeneous distribution of each element.

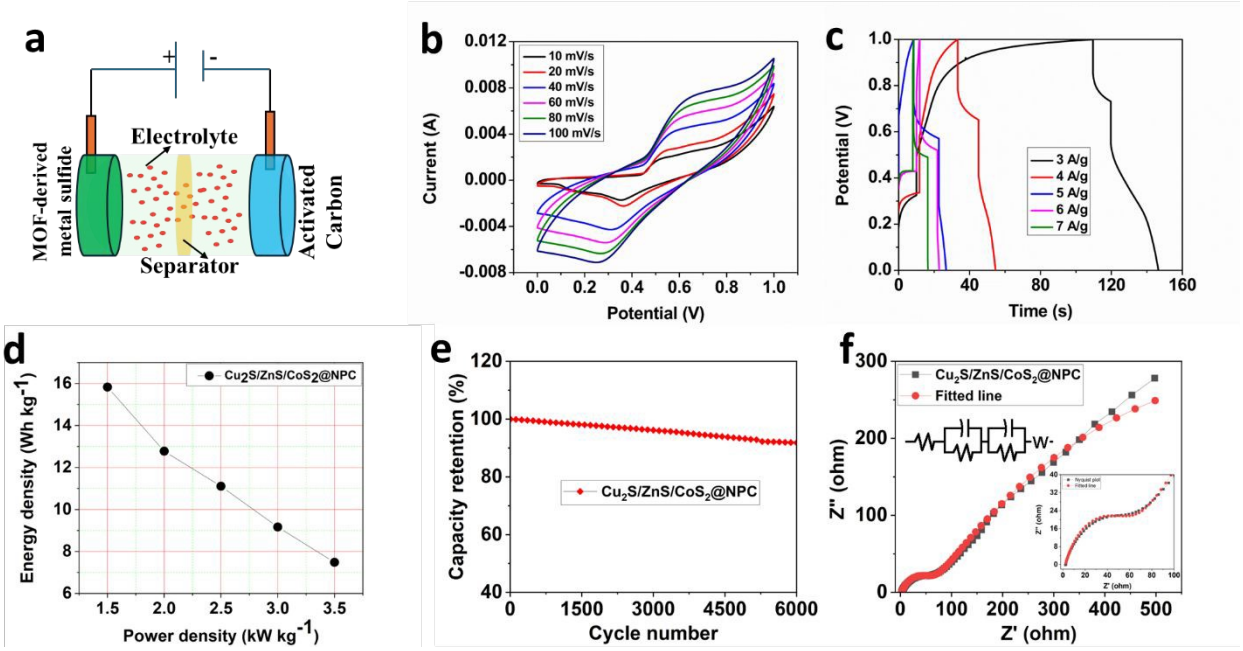

Figure 8. Asymmetric supercapacitor behavior using $Cu_2S/ZnS/CoS_2$@NPC as cathode: a) Graphical representation of device, b) CV profiles at different scan rates, c) GCD profiles at various current densities, d) Ragone plot, e) Cyclic stability. f) Nyquist plot.

Electrochemical OER Investigations

View Article Online
DOI: 10.1039/D6TA01424K

To investigate the OER potential and overpotential, the MOF-derived materials were evaluated via linear sweep voltammetry (LSV).[58] The LSV measurements were conducted at 10 mV s^{-1} in 1 M KOH electrolyte. The different electrolyte concentration was used than supercapacitor because it is the widely accepted standard electrolyte concentration for evaluating OER electrocatalysis. The iR uncompensated LSV profiles of all MOF-derived Cu/Zn/Co@NPC, $Cu_2Se/ZnSe/CoSe_2$@NPC, and $Cu_2S/ZnS/CoS_2$@NPC heterostructures are presented in **Figure 9(a)**. The calculated OER overpotential values at a current density of 10 mA cm^{-2} for the MOF-derived Cu/Zn/Co@NPC, $Cu_2Se/ZnSe/CoSe_2$@NPC, and $Cu_2S/ZnS/CoS_2$@NPC heterostructures are 230, 190, and 180 mV, respectively. Since most of the literature reports employed 85% iR compensation.[59] The 85% iR corrected LSV profiles for all of the MOF-derived Cu/Zn/Co@NPC, $Cu_2Se/ZnSe/CoSe_2$@NPC, and $Cu_2S/ZnS/CoS_2$@NPC heterostructures as displayed in **Figure 9(b)**. The evaluated overpotentials for Cu/Zn/Co@NPC, $Cu_2Se/ZnSe/CoSe_2$@NPC, and $Cu_2S/ZnS/CoS_2$@NPC heterostructures are 150, 140, and 120 mV at 10 mA cm^{-2}, respectively. The kinetic parameters are equally important with respect to the OER performance of the electrocatalysts and derivation of Tafel slope presented in supporting information.[60] Therefore, Tafel analysis was performed and the calculated values of the Tafel slopes were determined to be 180, 103, and 92 mV dec^{-1} for the Cu/Zn/Co@NPC, $Cu_2Se/ZnSe/CoSe_2$@NPC, and $Cu_2S/ZnS/CoS_2$@NPC heterostructures, respectively as shown in **Figure 9(c)**. The $Cu_2S/ZnS/CoS_2$@NPC heterostructure exhibit a lower Tafel slope indicating more facile kinetics for this electrocatalyst and suggests that it is the most efficient electrocatalyst among all of the materials reported here. The stability tests for the Cu/Zn/Co@NPC, $Cu_2Se/ZnSe/CoSe_2$@NPC, and $Cu_2S/ZnS/CoS_2$@NPC heterostructure materials were conducted at a fixed current density of 50 mA cm^{-2} for 30 hours and the curves demonstrate excellent stability which indicates the practical viability of the prepared materials as presented in **Figure 9(d)**. The TOF is of key importance in OER investigation in so far as it quantitatively demonstrates how many O_2 molecules are generated per active site per second. TOF values calculated were 0.00407, 0.00851, and 0.0123 s^{-1} for the Cu/Zn/Co@NPC, $Cu_2Se/ZnSe/CoSe_2$@NPC, and $Cu_2S/ZnS/CoS_2$@NPC heterostructures, see **Figure 9(e)**. The $Cu_2S/ZnS/CoS_2$@NPC heterostructure exhibits a higher TOF value indicating its superior intrinsic activity and efficient use of active sites for OER. This can be ascribed to the existence of a synergy between the multimetallic centers and conductive NPC framework. Moreover, the TOF results suggest that rational composition and effective heterostructure engineering can elevate the

View Article Online
DOI: 10.1039/D6TA01424K

catalytic kinetics of the designed materials. The comparative values of overpotentials for all materials investigated have been shown by bar plots as in **Figure 9(f)**.

The enhanced OER performance of the MOF-derived $Cu_2S/ZnS/CoS_2$@NPC heterostructure compared to that of Cu/Zn/Co@NPC and $Cu_2Se/ZnSe/CoSe_2$@NPC is primarily accredited to structure-driven properties. The sulfide-based frameworks when integrated with the conductive NPC network have higher electronic conductivity and provide a smoother pathway for electrons through the network and thus accelerate the charge transfer. Moreover, the multicomponent nature of the materials provides numerous heterointerfaces with staggered band alignments and local built-in fields which act to redistribute charge and optimize the adsorption energies of the reaction intermediates (OH*, O*, OOH*).[61, 62] Sulfides also undergo surface oxidation under anodic potential and generate catalytically active metal oxyhydroxide species which act as shells on the conductive sulfide core which are considered to be the true OER-active sites.[63] This core-shell framework supports facile electron transfer with an enhanced density of active sites. Additionally, the presence of multimetals and the MOF-derived synthetic strategy may introduce lattice strain and sulfur vacancies which can tune the d-band and create high energy adsorption sites for OH^-, consequently lowering the O-O bond formation barrier. These characteristics improve the mechanical as well as chemical robustness of the $Cu_2Se/ZnSe/CoSe_2$@NPC framework in alkaline media.

Notably, when the working potential of the supercapacitor exceeds the thermodynamic decomposition potential of water, the OER can occur at the positive electrode. As a result, water is continuously consumed while oxygen gas is generated. The formation of oxygen bubbles on the electrode surface can partially block electrolyte ion transport and may reduce the charge-discharge efficiency. Moreover, prolonged OER can also lead to oxidation of electrode materials, which may affect long-term stability and capacitive performance. In supercapacitor three-electrode measurements, the upper potential limit corresponds to 0.6 V vs. Ag/AgCl (≈1.64 V vs. RHE). Since the reported OER onset potential for the $Cu_2S/ZnS/CoS_2$@NPC catalyst is approximately 1.35 V vs. RHE, it is possible that partial OER contribution occurs when the potential exceeds this value. Therefore, a fraction of the measured current may originate from parasitic OER in addition to the capacitive charge storage process.[64]

Furthermore, EIS analysis was performed to gain greater insights into the charge transfer behavior of the Cu/Zn/Co@NPC, $Cu_2Se/ZnSe/CoSe_2$@NPC, and $Cu_2S/ZnS/CoS_2$@NPC heterostructures

View Article Online
DOI: 10.1039/D6TA01424K

at 0 V and 0.5 V (vs. RHE) under OER conditions as illustrated in **Figure 9(g, h, i)**. The inset of the Nyquist plot indicates the high-resolution EIS spectra at higher frequency for all heterostructures and reveals a well-defined semicircle at higher magnifications. The Nyquist plot at 0 V (vs. RHE) displayed no prominent semicircle for all heterostructures which indicates that capacitive behavior is dominant with no significant presence of Faradaic charge transfer behavior, suggesting the absence of electrochemical processes at this potential. On the other hand, at 0.5 V (vs. RHE), the appearance of a significant semicircle reflects a substantial increase in the R_{ct} due to surface oxidation and reformation processes. The appearance of semicircles indicates the transformation of pristine heterostructure surfaces into catalytically active metal (oxy)hydroxide phases which facilitate the OER phenomenon via adsorption and electron transfer by creating an interfacial layer.[65] The calculated R_{ct} and R_s values are 9.55, 59.62, 3.56, and 1.75, 1.79. 1.61 Ω for Cu/Zn/Co@NPC, Cu_2Se/ZnSe/$CoSe_2$@NPC, and Cu_2S/ZnS/CoS_2@NPC heterostructures, respectively. The lowest R_{ct} and R_s values for Cu_2S/ZnS/CoS_2@NPC confirmed the faster kinetics responsible for the enhanced OER activity.

Additionally, the capacitive behavior of the fabricated electrodes was estimated through the evaluation of EDLC. Therefore, CV profiles of the Cu/Zn/Co@NPC, Cu_2Se/ZnSe/$CoSe_2$@NPC, and Cu_2S/ZnS/CoS_2@NPC heterostructures were conducted in the non-Faradaic region (-0.3 to -0.2 V, *vs.* RHE) at various scan rates ranging from 100 mV s^{-1} to 500 mV s^{-1} and are displayed in **Figure S11(a, c, e)**. CV profiles of all heterostructures demonstrate a rectangular shape which is confirmation of electrochemical double layer formation during electrochemical analysis. However, there was a linear increase observed with increasing scan rate during anodic and cathodic current densities which indicates an increase in the electrochemically active surface area (ECSA). The C_{dl} values were calculated from non-Faradaic CV profiles by the slope of current density *vs.* scan rate plots and used for the calculations of ECSA. The evaluated C_{dl} values for the Cu/Zn/Co@NPC, Cu_2Se/ZnSe/$CoSe_2$@NPC, and Cu_2S/ZnS/CoS_2@NPC heterostructures are 1.16, 1.27, and 2.92 mF, respectively, see **Figure S11(b, d, f)**. The obtained C_{dl} values were used in the evaluation of the ECSA of all the heterostructures. Generally, specific capacitance of flat surfaces is considered to be in the region of 40 μF cm^{-2}.[66] The MOF-derived Cu/Zn/Co@NPC, Cu_2Se/ZnSe/$CoSe_2$@NPC, and Cu_2S/ZnS/CoS_2@NPC heterostructures exhibit ECSA's of 29, 31.8, and 73 cm^2, respectively. The Cu_2S/ZnS/CoS_2@NPC heterostructure has a higher ECSA which implies that this material provides more accessible active sites with enhanced OER activity.

View Article Online
DOI: 10.1039/D6TA01424K

These investigations provide an in-depth understanding that nanostructure engineering and design of the heterointerface impact the intrinsic kinetics and active sites of the MOF-derived Cu/Zn/Co@NPC, $Cu_2Se/ZnSe/CoSe_2$@NPC, and $Cu_2S/ZnS/CoS_2$@NPC heterostructures.

Additionally, the post-OER SEM images reveal the morphological stability of the catalysts after the OER as seen in **Figure S12**. The Cu/Zn/Co@NPC deposited on nickel foam, where a rough and interconnected nanostructured surface is preserved even after OER, indicating good structural integrity. Similarly, the $Cu_2Se/ZnSe/CoSe_2$@NPC electrode which maintains a porous and aggregated morphology, suggesting that the catalyst remains stable during electrochemical operation. The $Cu_2S/ZnS/CoS_2$@NPC also exhibits a relatively intact and porous architecture with slight agglomeration, which can facilitate electrolyte penetration and active site exposure. Overall, the SEM results confirm that the catalysts retain their hierarchical morphology after prolonged OER testing, demonstrating good durability and structural robustness. The post-OER XPS analysis of the MOF-derived $Cu_2S/ZnS/CoS_2$@NPC heterostructure to investigate the surface chemical states after catalytic activity as shown in **Figure S13**. The survey spectrum confirms the presence of Cu, Zn, Co, S, C, N, and K elements in the catalyst. The high-resolution spectra of Cu 2p, Zn 2p, and Co 2p reveal the characteristic peaks corresponding to their respective metal states, indicating that the metal sulfide framework remains stable after OER. S 2p verifies the presence of metal-sulfur bonding in the heterostructure. The C 1s and N 1s spectra confirm the existence of NPC that enhances electrical conductivity and structural stability. Additionally, the K 2p peak originates from the electrolyte residue after OER testing. The XPS results suggest that the catalyst maintains its chemical composition and active structure after prolonged OER operation.

View Article Online
DOI: 10.1039/D6TA01424K

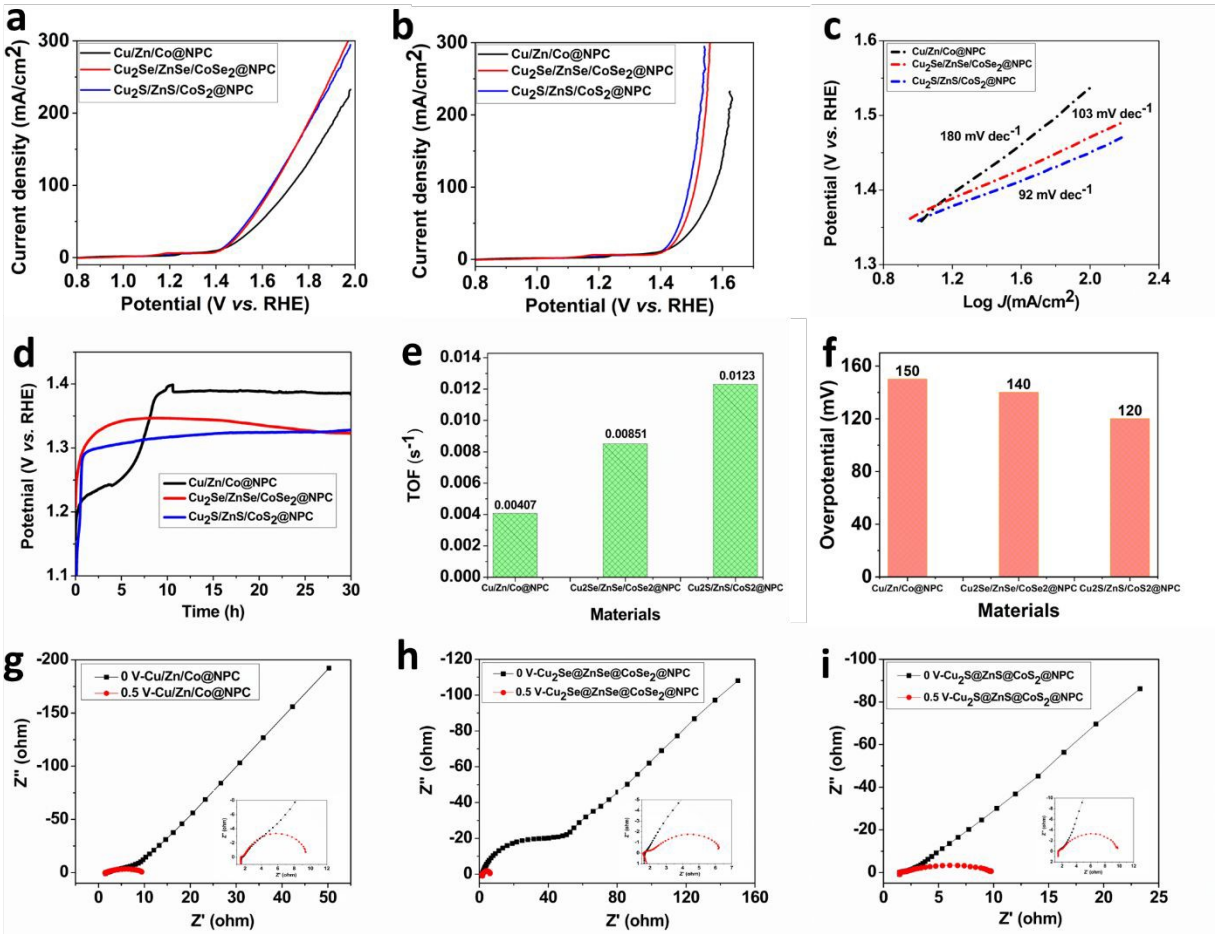

Figure 9. Electrochemical OER investigations of the synthesized materials: a) iR uncompensated LSV profiles, b) iR compensated LSV, c) Tafel plots with calculated slope values, d) Stability curves at 50 mA, e) TOF, f) Comparison of overpotentials at 10 mA cm^{-2}, and g, h, i) Nyquist plots recorded at 0 and 0.5 V (vs. RHE) under OER conditions.

Conclusions

This study has demonstrated the successful synthesis of MOF-derived Cu/Zn/Co@NPC, $Cu_2Se/ZnSe/CoSe_2$@NPC, and $Cu_2S/ZnS/CoS_2$@NPC heterostructures and the effectiveness of the MOF-derived strategies to develop multifunctional electrodes for integrated energy storage and conversion applications. Among the developed materials, $Cu_2S/ZnS/CoS_2$@NPC exhibits the highest specific capacitance of 1206 F g^{-1} at 1 A g^{-1}, outperforming Cu/Zn/Co@NPC and $Cu_2Se/ZnSe/CoSe_2$@NPC. An asymmetric supercapacitor device assembled using $Cu_2S/ZnS/CoS_2$@NPC achieves a specific capacitance of 114 F g^{-1} at 3 A g^{-1} and delivered an energy density of 15.83 Wh kg^{-1} at a power density of 1.5 kW kg^{-1} with capacity retention of 92.1%

View Article Online
DOI: 10.1039/D6TA01424K

over 6000 cycles. Moreover, Cu/Zn/Co@NPC, $Cu_2Se/ZnSe/CoSe_2$@NPC, and $Cu_2S/ZnS/CoS_2$@NPC exhibited low overpotentials of 150, 140, and 120 mV at 10 mA cm^{-2} with Tafel slopes of 180, 103, and 92 mV dec^{-1}, respectively. The excellent electrochemical performance of the sulfide-based $Cu_2S/ZnS/CoS_2$@NPC heterostructure is attributed to synergistic multimetallic composition, a conductive NPC framework, and well-organized heterointerfaces. Our findings on these electrode systems highlight the promising potential of MOF-derived multimetal chalcogenides to act as bifunctional electrode materials for energy storage and electrocatalytic applications. Future developments should focus on interfacial investigations to enhance the charge-transfer kinetics, dynamic structural evolution via in-situ/operando techniques, and device-level integration in asymmetric SCs and water-splitting systems to assess their practical feasibility.

Author contributions

Muhammad Nasir Hussain: Resources, Investigation, Conceptualization, Methodology, writing-original draft, Writing-review & editing, **Nesrin Bugday:** Resources, Investigation, Conceptualization, Methodology, writing-original draft, **Stephen G. Hickey:** Investigation, Methodology, writing-original draft, Writing-review & editing, **Umair Shamraiz:** Conceptualization, Formal Analysis, Writing-original draft, Writing-review & editing, **Christopher A. Howard**: Methodology, writing-original draft, Writing-review & editing, **Xiaobo Ji:** Investigation, Methodology, writing-original draft, **Sedat Yaşar:** Resources, Investigation, Conceptualization, Methodology, writing-original draft, Writing-review & editing.

Declaration of Competing Interest

The authors declare that they have no known competing financial interests or personal relationships that could have appeared to influence the work reported in this paper.

Data Statement

Data will be made available on request.

Acknowledgments

This work was supported by the BAP Unit of İnönü University with the project number FBG-2023-3310 and FOA-2025-4310.

View Article Online
DOI: 10.1039/D6TA01424K

References

1. X. F. Lu, Y. Fang, D. Luan and X. W. D. Lou, *Nano Lett.,* 2021, **21,** 1555-1565.
2. R. Xu, L. Du, D. Adekoya, G. Zhang, S. Zhang, S. Sun and Y. Lei, *Adv. Energy Mater.,* 2021, **11,** 2001537.
3. C. V. V. Muralee Gopi, S. Alzahmi, V. Narayanaswamy, R. Vinodh, B. Issa and I. M. Obaidat, *J. Energy Storage.,* 2025, **114,** 115729.
4. B. C. Yallur, M. P. Rao, M. Harshitha, D. Basrur, P. H. Umesh, V. Kamat, K. D. Venu Prasad, K. N. Venugopala and R. S. Bhat, *Adv. Sustain. Syst.,* 2025, **9,** 2500121.
5. M. N. Hussain, A. Inayat, S. M. Shah, M. Ihsun, A. Haider, S. M. Abbas and S. G. Hickey, *Nanoscale.,* 2025, **17,** 25846-25858.
6. Z. Han, R. Fang, D. Chu, D.-W. Wang and K. Ostrikov, *Nanoscale Adv.,* 2023, **5,** 4015-4017.
7. M. Libber, N. Gariya and M. Kumar, *J. Solid State Electrochem.,* 2025, **29,** 513-527.
8. P. S. Nanda, A. Gautam, A. K. Singh and R. S. Singh, *J. Energy Storage.,* 2025, **131,** 117431.
9. S. Singha Roy, S. Nagappan, A. K. Satheesan, A. Karmakar and S. Kundu, *J. Phys. Chem. C.,* 2024, **128,** 13634-13650.
10. N. Jiang, Z. Zhu, W. Xue, B. Y. Xia and B. You, *Adv. Mater.,* 2022, **34,** 2105852.
11. D. Mladenović, A. Mladenović, D. M. Santos, A. B. Yurtcan, Š. Miljanić, S. Mentus and B. Šljukić, *J. Electroanal. Chem.,* 2023, **946,** 117709.
12. M. Trębala and A. Łamacz, *Molecules.,* 2025, **30,** 1656.
13. H. Liu, R. Xiong, S. Ma, R. Wang, Z. Liu, T. Yao and B. Song, *Energy Adv.,* 2025, **4,** 55-83.
14. Y. Liu, Y. Jia, H. Jia and L. Gao, *Molecules.,* 2025, **30,** 3238.
15. L. Chen, Y. Liu, H. Cong, Q. Ge, W. Zhao, N. Jiang and Q. Zhang, *Mater. Chem. Front.,* 2024, **8,** 986-1014.
16. X. Liu, M. Albloushi, M. Galvin, C. W. Schroeder, Y. Wu and W. Li, *Green Chem.,* 2024, **26,** 11351-11363.
17. L. Gao, Y. Yao, Y. Ma, J. Huang, Y. Chen, L. Chen and L. Jia, *Adv. Funct. Mater.,* 2025, **35,** 2507282.

View Article Online
DOI: 10.1039/D6TA01424K

18. M. Afshan, S. Das, D. Rani, S. Sharangi, H. E. M, M. Pahuja, S. A. Siddiqui, S. Rani, N. Chaudhary and Jyoti, *ACS Appl. Mater. Interfaces.,* 2025, **17,** 23892-23910.
19. J. da Silva Hortêncio, R. A. Raimundo, A. J. Araújo, A. L. M. de Oliveira, D. A. Macedo, S. G. Lemos and F. F. da Silva, *ChemistryOpen.,* 2025, **14,** e202500180.
20. A. Al Mahmud, A. H. Alshatteri, H. S. Alhasan, W. Al Zoubi, K. M. Omer and M. R. Thalji, *Electrochim. Acta.,* 2024, **503,** 144857.
21. J. Li, Q. Yu, L. Shi and X. Wei, *J. Electroanal. Chem.,* 2025, **997,** 119482.
22. D. Cai, Z. Yang, R. Tong, H. Huang, C. Zhang and Y. Xia, *Small.,* 2024, **20,** 2305778.
23. A. Karimi, A. A. Ensafi and B. Rezaei, *Fuel.,* 2023, **334,** 126536.
24. F. Mousavi, S. Ghasemi and M. Shamsipur, *Energy & Fuels.,* 2024, **38,** 23101-23113.
25. Y. Li, F. Wu, J. Qian, M. Zhang, Y. Yuan, Y. Bai and C. Wu, *Small Sci.,* 2021, **1,** 2100012.
26. J. Lu, H. Jiang, P. Guo, J. Li, H. Zhu, X. Fan, L. Huang, J. Sun and Y. Wang, *Electrochim. Acta.,* 2024, **507,** 145122.
27. S. Khan, N. Ullah, A. Mahmood, M. Saad, Z. Ullah, W. Ahmad and S. Ullah, *Energy Technol.,* 2023, **11,** 2201416.
28. H. Guo, Y. Liu, H. Ren, Y. Hao, L. Peng and W. Yang, *J. Alloys Compd.,* 2025, **1029,** 180765.
29. Y. Tang, J. Li, Z. Lu, Y. Wang, K. Tao and Y. Lin, *Nanomaterials.,* 2023, **13,** 2621.
30. Y. Chen, Y. Zhao, W. He, Y. Liu, H. Xing, X. Zhu, Y. Guo, J. Feng, C. Liao and Y. Zong, *Mater. Today Commun.,* 2023, **37,** 106955.
31. M. Maniyazagan, E. Shanmugasundaram, P. Naveenkumar, K. P. Nithyanandam, H.-W. Yang, S. Thambusamy and S.-J. Kim, *J. Power Sources.,* 2025, **647,** 237379.
32. J. Hou, Z. Huang, H. Lu, C. Chen, X. Wu, Y. Xiao, W. Wei, M. Xue, Y. Ma and X. Ma, *J. Mater. Chem. A.*, 2025, **13,** 25042-25053.
33. I. Hussain and K. Zhang, Nanoscale, 2024, **16,** 15515-15528.
34. K. C. Majhi and M. Yadav, *ACS Eng. Au.,* 2023, **3,** 278-284.
35. N. Bugday, A. A. Genc, W. Bouali, N. Erk and S. Yaşar, *Electrochim. Acta.,* 2025, **536,** 146715.
36. K. Cheirmadurai, S. Biswas, R. Murali and P. Thanikaivelan, *RSC Adv.,* 2014, **4,** 19507-19511.

View Article Online
DOI: 10.1039/D6TA01424K

37. B. Hoogendoorn, M. Parra, A. Capezza, Y. Li, K. Forsberg, X. Xiao and R. Olsson, *Mater. Adv.,* 2023, **4,** 2683-2683.
38. S.-M. Zhou, S.-Y. Lou, Y.-Q. Wang, X.-L. Chen, L.-S. Liu and H.-L. Yuan, *Nanoscale Res. Lett.,* 2011, **6,** 285.
39. W. Xie, F. Liu, Y. Zheng, N. Ge, B. Dai and X. Zhang, *RSC adv.,* 2022, **12,** 14112-14118.
40. M. Jia, Y. Jin, C. Zhao, P. Zhao and M. Jia, *J. Alloys Compd.,* 2020, **831,** 154749.
41. M. Muska, J. Yang, Y. Sun, J. Wang, Y. Wang and Q. Yang, *ACS Appl. Nano Mater.,* 2021, **4,** 5796-5807.
42. K. Purushothaman and B. Sethuraman, *Appl. Phys. A.,* 2025, **131,** 749.
43. A. Tamilselvan, S. Sengupta, A. Pramanik, P. M. Ajayan and M. Kundu, *J. Mater. Sci.,* 2025, **60,** 2709-2709.
44. K. Shwetha, M. S. Kamath, C. K. Rastogi, Y. Athreya, S. Sudhakaran and C. Manjunatha, *J. Energy Storage.,* 2024, **97,** 112699.
45. N. Bugday, W. Deng, O. Duygulu, G. Zou, H. Hou, X. Ji and S. Yaşar, *Rare Met.,* 2025, **44,** 9920-9937.
46. R. Xu, M. Arif, G. Pan, L. Xu and T. Zhu, *Nanoscale Adv.,* 2025, **7,** 5058-5066.
47. G. Wang, B. Huang, Z. Li, Z. Lou, Z. Wang, Y. Dai and M.-H. Whangbo, *Sci. Rep.,* 2015, **5,** 8544.
48. X. Zhang, Y. Yang, P. Jia, S. Li, J. Su, S. Lv, Y. Sun, R. Liu, Y. Xu and W. K. Pang, *J. Power Sources.,* 2025, **644,** 237117.
49. X. Liu, L. Yan, S. Sun, J. Du and S. Yin, *ACS Appl. Energy Mater.,* 2025, **8,** 10071-10081.
50. J. Zhu, D. Mo, L. Tao, J. Li, S. Fu, L. Dong, B. Li, Z. Chen and M. Fan, *J. Environ. Chem. Eng.,* 2023, **11,** 111218.
51. M. N. Hussain, A. Naveed, M. Sohail, M. D. Khan, S. G. Hickey, N. Ullah, I. Ahmad, A. Haider and S. M. Shah, *ACS Appl. Eng. Mater.,* 2025, **3,** 1315-1326.
52. M. Ye, H. Hou, X. Liu, Z. Sun, X. Yu and J. Rong, *J. Mol. Struct.,* 2025, **1323,** 140774.
53. P. Naveenkumar, P. Rajkumar, M. Maniyazagan, K. Nithyanandam, H.-W. Yang, J. Kim and S.-J. Kim, *J. Electroanal. Chem.,* 2025, **996,** 119328.
54. X. Li, W. Zhang, Z. Gu, Q. Cai, H. Kang, B. Yang and Z. Li, *Electrochim. Acta.,* 2025, **509,** 145312.

View Article Online
DOI: 10.1039/D6TA01424K

55. P. Sivakumar, J. Balamurugan, C. J. Raj, P. Subramanian, A. D. Savariraj, R. Manikandan and H. Jung, *J. Mater. Chem. A.,* 2025, **13,** 5961-5973.
56. W. G. Nunes, B. G. Freitas, R. M. Beraldo, R. M. Filho, L. M. Da Silva and H. Zanin, *Sci. Rep.,* 2020, **10,** 19195.
57. M. Shahzad, F. Ahmad, M. Ibraheem, A. Shakoor, S. M. Ramay, M. R. Raza and S. Atiq, *RSC adv.,* 2025, **15,** 6308-6323.
58. S. Yu, D. Liu, C. Wang, J. Li, R. Yu, Y. Wang, J. Yin, X. Wang and Y. Du, *J. Colloid Interface Sci.,* 2024, **653,** 1464-1477.
59. Y. J. Son, R. A. Marquez, K. Kawashima, L. A. Smith, C. E. Chukwuneke, J. Babauta and C. B. Mullins, *ACS Energy Lett.,* 2023, **8,** 4323-4329.
60. J. Liang, T. Lei, Y. Zhang, Y. Yuan, G. Yang and L. Zhang, *ACS Appl. Mater. Interfaces.,* 2025, **17,** 48220-48230.
61. Z. Fei, Y. Song, M. Wu, Y. Wu, Y. Chen, D. J. Kang, C. Bian and Y. Qian, *Catalysts.,* 2025, **15,** 928.
62. H. Adamu, Z. H. Yamani and M. Qamar, Mater. *Renew. Sustain. Energy.,* 2022, **11,** 169-213.
63. M. Wang, C.-L. Dong, Y.-C. Huang and S. Shen, *ACS Catal.,* 2020, **10,** 1855-1864.
64. Q. Lu, T. Zhou, M. Chen, H. Sun and Q. Liu, *Coord. Chem. Rev.,* 2026, **550,** 217389.
65. U. Shamraiz, A. Badshah and N. u. Ain, *ACS Appl. Energy Mater.,* 2023, **6,** 2489-2496.
66. Y. Wang, Z. Ge, X. Li, J. Zhao, B. Ma and Y. Chen, *J. Colloid Interface Sci.,* 2020, **567,** 308-315.

View Article Online
DOI: 10.1039/D6TA01424K

Data Statement

Data are available upon request from the authors.